Tough silicon carbide macro/mesocellular crack-free monolithic foams

Simona Ungureanu, Gilles Sigaud, Gerard L. Vignoles, Christophe Lorrette, Marc Birot, Alain Derré, Odile Babot, Hervé Deleuze, Alain Soum, Gilles Pécastaings, et al.

Tough silicon carbide macro/mesocellular crack-free monolithic foams

Simona Ungureanu,[ab] Gilles Sigaud,[a] Gérard L. Vignoles,[c] Christophe Lorrette,[d] Marc Birot,*[b] Alain Derré,[a] Odile Babot,[b] Hervé Deleuze,[b] Alain Soum,[e] Gilles Pécastaings[e] and Rénal Backov*[a]

Taking the benefit of Si(HIPE) as a hard monolithic template to shape macro-mesoporous foams by using polycarbosilane as pre-ceramic precursor β-SiC, macro/mesocellular foams have been synthesized. Both macroscopic Plateau border morphology and final mechanical properties can be tuned through varying the starting amount of polycarbosilane precursor. Resulting silicon carbide foams, labeled SiC(HIPE), are composed of β-SiC at the microscopic length scale, while bearing 110 $m^2 g^{-1}$ as specific area at the mesoscopic length scale, and up to 92% of macroporosity. The as-synthesized crack-free SiC(HIPE) monolithic foams are associated with outstanding mechanical properties as, for instance, 50–58 MPa of compression Young modulus. The thermal behaviors of these foams are assessed with bulk heat capacities comprising between 0.15 J $g^{-1} K^{-1}$ to 0.55 J $g^{-1} K^{-1}$ that decrease when the foam porosity increases, while their heat conductivities are following the same rules ranging from 2.6 to 4.6 W $m^{-1} K^{-1}$.

1. Introduction

Nowadays chemists are required to envisage materials that are more and more complex in nature and structure, bearing multi-functionality and, at the extreme, being able to develop some degree of autonomy, taking inspiration from living organisms. To construct materials exhibiting such performance, chemical science cannot be restricted to a single specific domain of chemistry but has to be addressed through a strong interdisciplinary approach, thereby crossing chemical boundaries and beyond. In such a context, innovative synthetic pathways are certainly reaching the notion of "complexity".[1] When it comes to the chemistry of materials, there is a crucial need for a "rational design" where the final enhanced functionality or real competitive application to be reached will ensure the overall synthetic pathway to be applied. From this way of thinking there has recently emerged the concept of *Integrative Chemistry*.[2] This new transversal domain of chemical science can be defined as an "interdisciplinary tool box" where advanced functional materials bearing hierarchical structures can be tailor-made *via* the smart integration of soft chemistry-based pathways and the versatile processing conditions offered by soft-matter physical-chemistry. One synthetic path combines sol–gel chemistry with lyotropic mesophases and concentrated direct emulsions to promote either inorganic Si(HIPE)[3] or hybrid organic–inorganic foams called Organo-Si(HIPE)[4] (the acronym HIPE refers to High Internal Phase Emulsion). In any circumstances, if the micro-/meso-porosities offer molecular reactivity through diffusion or dispersion phenomena,[5] some macroporosity where the fluid hydrodynamics are driven by the Darcy law[6] is also necessary to limit the diffusion path (and associated low kinetics). This provides fast accessibility to the reactive centers and eases removal of the electrolytes, catalyzed species, or purified solvent when dealing with electrodes, catalysts, or membranes respectively.[7–9] Thereby, in monolith-shaped materials, hierarchical porosity with an interconnected macroporosity appears to be of essential importance. Recently, we used silica macrocellular foams, labeled Si(HIPE), as a hard template to produce the parent carbonaceous macrocellular foams, labeled Carbon (HIPE),[10] bearing standard application in Li-ion electrodes and chemical electro-capacitor devices, while promoting outstanding capabilities when used as bio-electrocatalysts when functionalized with specific enzymes.[11,12] Beyond carbon, silicon carbide (SiC) is an important non-oxide ceramic associated with a set of unique properties such as high thermal stability, high heat conductance addressed through small heat expansion, endurance toward high temperature oxidation and corrosion, overall

aUniversite de Bordeaux, Centre de Recherche Paul Pascal, UPR 8641 CNRS, 115 avenue Albert Schweitzer, 33600 Pessac, France. E-mail: backov@crpp-bordeaux.cnrs.fr
bUniversite de Bordeaux, Institut des Sciences Mol eculaires (ISM) UMR 5255 CNRS, 351 Cours de la Lib eration, 33405 Talence, France. E-mail: m.birot@ism.u-bordeaux1.fr
cUniversite de Bordeaux, Laboratoire des Composites Thermostructuraux, UMR 5801 CNRS-UBI-CEA-Snecma Propulsion Solide, 3 All ee de la Bo etie, 33600 Pessac, France
dCEA, Laboratoire des Composites Thermostructuraux, UMR 5801 CNRS-UBI-CEA-Snecma Propulsion Solide, 3 All ee de la Bo etie, 33600 Pessac, France
eUniversite de Bordeaux, Laboratoire de Chimie des Polym eres Organiques UMR 5629 CNRS, ENSCBP 16 avenue Pey Berland, BP 108, 33607 Pessac, France

chemical inertness and bearing semiconductor behavior at high temperature.[13–15] There are mainly two crystallographic forms of SiC: the high temperature (>1500 °C) hexagonal α-phase that presents two commercially available polytypes, namely 4*H*- and 6*H*-SiC; and the low temperature form (< 1500 °C) cubic β-phase.[16] Usually, α-SiC, prepared by the Acheson process patented in 1892,[17] which manufacturers still rely on today, is obtained as a powder which cannot be sintered to dense films and bodies, and an alternative method had to be developed. Also, the pyrolysis of polycarbosilane, at temperatures close to 1400 °C under a reductive atmosphere, generates β-SiC.[18] Among different ways to produce porous SiC, nanocasting makes use of a preformatted porous silica hard template impregnated with a pre-ceramic polymer that is subsequently heated under a non-oxidative atmosphere, followed by the exotemplate removal. Final SiC materials may be mesoporous,[19] macroporous,[20] or even hierarchically organized while being monolithic.[21] If hierarchical porosity is an important characteristic, considering the above-mentioned hydrodynamic issues, the monolith's final mechanical robustness[22,23] is a *sine qua non* property in order to fit integration of the as-synthesized SiC porous materials into a device set-up.

In this study we used Si(HIPE) as a hard template to shape macro-mesoporous foams by using polycarbosilane as a pre-ceramic precursor. The resulting silicon carbide foams, labeled SiC(HIPE), were characterized by electron microscopy, mercury intrusion, nitrogen sorption, XRD and compression mechanical tests.

2. Experimental

Materials

Polycarbosilane (PCS) (average molecular weight: 1500–2500) was purchased from NaBond. Tetradecyltrimethylammonium bromide 98% (TTAB) was purchased from Alfa Aesar. Tetraethylorthosilicate 98% (TEOS) was purchased from Aldrich. Acetone and dodecane 99% were purchased from Rectapur. Tetrahydrofuran (THF), hydrofluoric acid 48% (HF), and hydrochloric acid 37% (HCl) were purchased from VWR (AnalaR Normapur grade). The reactants were used as received without further purification

Synthetic pathway

Si(HIPE) synthesis. Typically, TEOS (5 g) was added to an aqueous solution of TTAB (16 g, 35 wt%) that had previously been acidified with 7 g of HCl. Hydrolysis was carried out until a monophasic medium was obtained. The oily phase, dodecane (35 g), was then emulsified drop by drop into the hydrophilic continuous phase using a mortar, and the emulsion was allowed to condense for 1 week at room temperature. The as-synthesized monoliths were washed three times with a THF/acetone mixture (1 : 1 v/v) to extract the oily phase. Drying of the materials for a week at room temperature was followed by thermal treatment at 650 °C (heating rate of 2.8 °C min^{-1}) for 6 h, with a 2 h plateau at 200 °C to remove TTAB. Full silica template characterization can be found elsewhere.[3]

SiC foams synthesis. A monolith of Si(HIPE) (0.5 g) was added into 20, 30, 40 and 60 wt% PCS solutions in THF (30 mL). For a good impregnation, the suspension was placed under dynamic vacuum until the effervescence disappeared. After 3 days of aging at room temperature under static vacuum, the solution was filtered and the monolith was rinsed with THF and dried in an air oven at 100 °C overnight. Then, each monolith underwent two thermal treatments under an argon atmosphere. First, the acquired PCS/silica composite was heated at 1000 °C for 2 h with a plateau at 300 °C for 5 h (heating rate of 2 °C min^{-1}) and a second plateau at 700 °C (heating rate of 0.5 °C min^{-1}) for cross-linking and pyrolyzing the PCS. In the second treatment, the temperature was raised to the final value for carbidization: 1300 °C for 2 h with a heating rate of 2 °C min^{-1}. The resulting SiC/silica composites were washed with 10 wt% aqueous hydrofluoric acid several times to remove the silica template. The as-synthesized materials were named SiC-20, SiC-30, SiC-40 and SiC-60, respectively.

Characterizations

Scanning electron microscopy (SEM) observations were performed using a Hitachi TM-1000 apparatus at 15 kV. Transmission electron microscopy (TEM) experiments were performed with a Jeol 2000 FX microscope (accelerating voltage of 200 kV). Intrusion/extrusion mercury measurements were performed using a Micromeritics Autopore IV porosimeter to reach the scaffold's macrocellular characteristics. Surface-area and pore characteristics on a mesoscale were obtained using a Micromeritics ASAP 2010 apparatus. To obtain the small angle X-ray scattering (SAXS) information, the scattered radiation was collected on a two-dimensional detector (Imaging Plate system from Mar Research, Hamburg). The sample to detector distance was 500 mm. X-Ray diffraction (XRD) experiments were carried out on a PANalytical X'pert MPD diffractometer with Bragg–Brentano θ–θ geometry, Cu-Kα1 radiation (40 kV, 40 mA, λ_{Cu} = 1.5418 Å). Thermogravimetric analyses (TGA) were carried out under an oxygen flow (5 mL min^{-1}) using a heating rate of 5 °C min^{-1}. The apparatus was a Setaram TAG-16 thermogravimetric analyzer. Transmission IR spectra were obtained from KBr pellets using a Nicolet 750 FTIR spectrometer. The mechanical properties of the samples were obtained using an Instron 4466 mechanical-testing machine. The specimens were compressed between two rigid plates and deformations at various loads were recorded. The crosshead speed was set at 0.5 mm s^{-1}. X-Ray photoelectron spectroscopy (XPS) experiments were performed using Escalab VG 220i XL apparatus. Thermal analyses to obtain the foam calorific capacities (c_p) were conducted using the modulated temperature mode of a TA-Q2000 DSC apparatus. Thermal conductivities were estimated using a heating laser source (Melles Griot 85 BCA series, 5 mW @ 473 nm) and an IR camera (Cedip FLIR SC 7000). The sample surface was subjected to a laser step impulse, and the front surface temperature was recorded as a function of time. The frame rate was 100 per second, and the pixel size was 0.155 μm.

3. Results and discussion

Considering the whole synthetic path (Scheme 1) we firstly synthesized silica Si(HIPE) matrices bearing macroporous, interconnected void spaces in a monolithic shape making use of

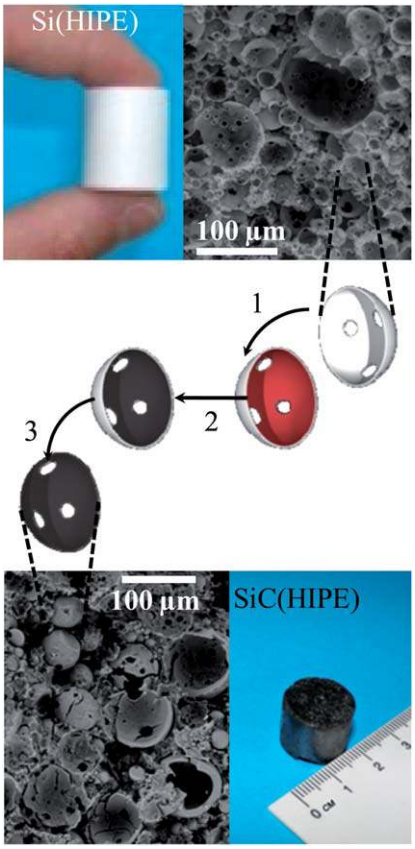

Scheme 1 Overall integrative chemistry-based synthetic employed to generate β-SiC macrocellular foams, SiC(HIPE): **1** PCS infiltration and pre-polymerization steps, **2** carbidization, **3** silica removal through HF treatment.

the sol–gel process and using emulsion and lyotropic mesophases as soft templates.[3]

Secondly, a one-step macro-casting process was employed where the starting silica foam was impregnated with a solution of PCS dissolved in anhydrous THF, followed by a pyrolysis step at 1000 °C. Finally, carbidization of PCS was achieved at 1300 °C under an argon atmosphere, while the native silica framework was vanished through hydrofluoric acid (HF) washing. The as-synthesized materials were labeled SiC-*X*, where *X* is defining the starting PCS wt% (see synthetic routes for details). Considering SEM (Fig. 1) we observed that the overall macroscopic textures of final SiC(HIPE) monolithic foams are retained after the carbidization process and the typical hollow-sphere aggregated structure of the native Si(HIPE) is lost,[3] when increasing the amount of starting PCS wt%.

For instance, it is clear that the foams SiC-20 and SiC-30 (Fig. 1a and 1b) are depicting the typical aggregated hollow-sphere morphology, while the foams SiC-40 and SiC-60 bear a more continuous skeleton (Fig. 1c and 1d). This evolution of topology is different from what we observed recently when generating carbonaceous foams Carbon(HIPE)[10] through the same impregnation path, where the wall thickness was increasing when increasing the starting formaldehyde-resorcinol wt%, but the aggregated hollow-sphere morphology was maintained. This difference of topology evolution is indeed important because for the Carbon(HIPE) the solution of formaldehyde-resorcinol

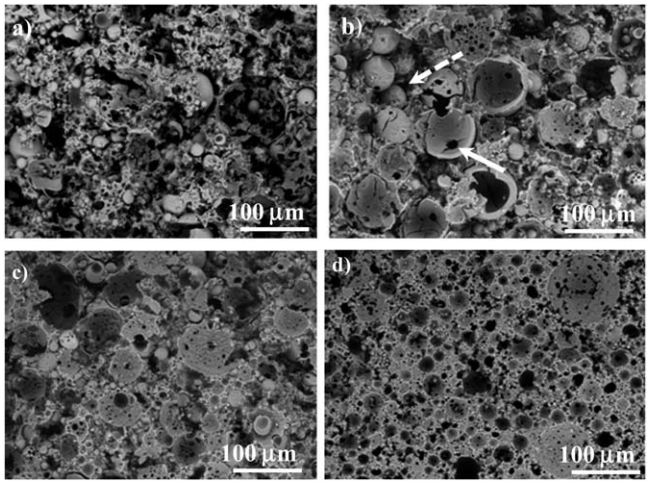

Fig. 1 SEM micrographs of the SiC(HIPE) when increasing the starting PCS wt%: (a) SiC-20, (b) SiC-30, (c) SiC-40, (d) SiC-60. The plain white arrow indicates internal cell junctions, while the dashed white arrow indicates the external junction emerging from macroscopic adjacent cell interstices.

dissolved in THF was not wetting the macroporous surface and thereby was not accessing the silica hard template mesoscopic void spaces. Here, the fact that the texture changes from an aggregated morphology for the lowest PCS wt% toward a more continuous wall aspect for the highest PCS wt% can be explained by the fact that the starting PCS-THF solution is wetting the silica macroporous walls, but it is also impregnating the silica wall mesoporosity at least partially. In order to better qualify and quantify the macroporosity, mercury porosimetry investigations were performed (Fig. 2).

The first important feature is that these SiC(HIPE) are robust enough to endure mercury impregnation without collapsing. Also, we have to bear in mind that mercury porosimetry measurements are providing diameters of the void spaces limiting the mercury impregnation, this is to say the windows that connect adjacent cells and not the cells themselves. In Fig. 2 we can notice that the cell windows are rather polydisperse, ranging from 0.1 µm to 10 µm, and emerge from the combination of two connecting windows, previously named external (bigger) and internal cell junctions (smaller),[3,10] where these junctions can be seen in Fig. 1b. Something important to note is that the junction diameters are decreasing when increasing the starting PCS wt%. This feature can be explained with two cooperative phenomena when the PCS wt% increases: the increase of wall thickness and, certainly more importantly, the simultaneous gain of higher walls continuity where the external cell junctions are more and more lost. As a direct consequence, the SiC-60 cell junction diameters are squeezed within the 0.1–1 µm scale only, where all the bigger cell junctions (external) are cancelled. Overall, both mercury intrusion volume and the macroscopic porosity decreases from the SiC-20 to the SiC-60 monolithic foams (Table 1).

These effects are expected because the PCS wt% is increasing from SiC-20 to SiC-60, while the starting full void space of the Si (HIPE) exotemplate remains constant. In addition, we can observe that the skeleton density is decreasing when increasing the PCS wt%. Normally, the skeletal density should remain at a constant value inferior to the SiC density (around 3.2 g cm^{-3}).

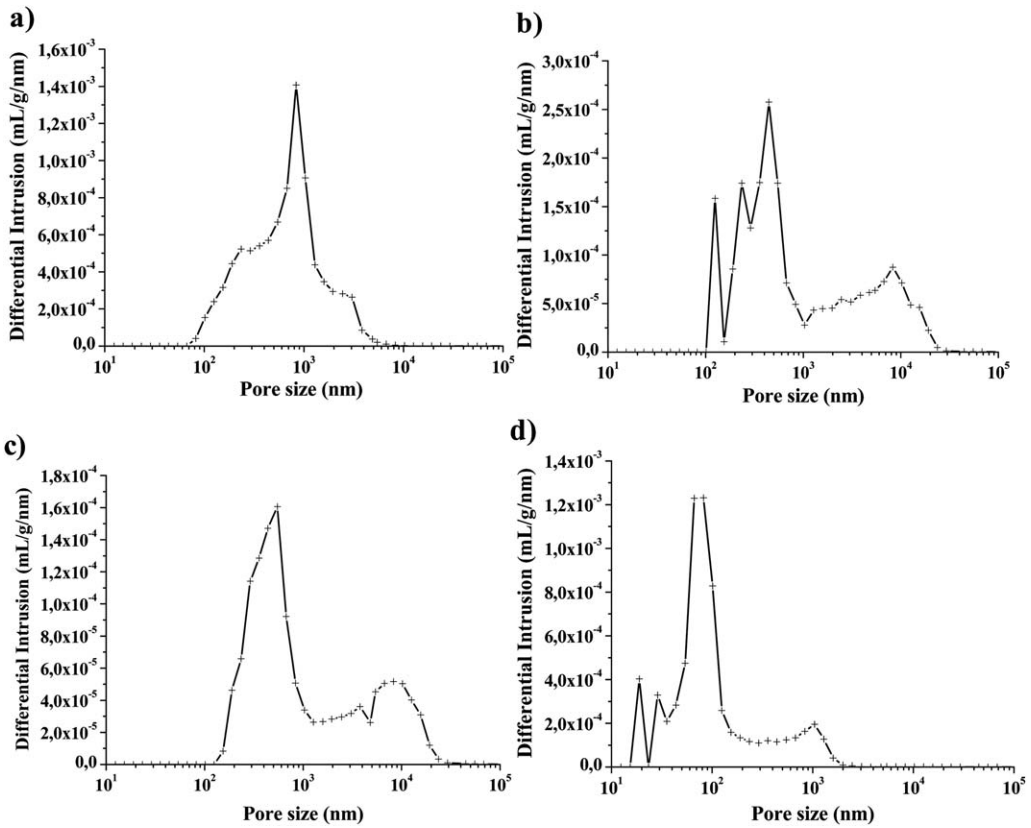

Fig. 2 Macroscopic pore size distribution obtained through mercury intrusion porosimetry: (a) SiC-20, (b) SiC-30, (c) SiC-40, (d) SiC-60.

The value should be inferior to the skeletal SiC density because it is well known that mercury porosimetry does not assess micro- and meso-porosities. As a direct consequence, the density value should be the SiC density minimized by the wall mesoscopic void spaces. It means that, as the precursor concentration increases, the precursor impregnation within the starting Si(HIPE) mesoporosity is increasing, too. This effect is certainly due to Fick diffusion within the starting silica foam mesoporosity, the diffusion being enhanced when the precursor concentration is increased. If this scenario is correct, then the mesoporosity should be optimized as the concentration of the carbosilane precursor increases. Indeed, as it will be discussed within the next section, the mesoporosity (BJH) is also increasing when increasing the PCS wt%. This overall scheme certainly explains the skeleton density evolution with the starting PCS wt%.

These SiC(HIPE) foams have been characterized and quantified using nitrogen sorption experiments and TEM. As observed within Fig. 3, all the foams are bearing more or less the same type II–IV isotherms, characteristic of macroporous systems bearing some mesoporosity.

These macrocellular foams do not depict any sign of microporosity and are essentially macroporous, as demonstrated with the mesoscopic pore size distribution obtained through density functional theory (Fig. 4).

Whatever the SiC(HIPE), we can observe that the porosity is spread from 15–20 Å to 1000 Å, with a maximum around 50 Å. Considering Table 2 we can notice a weak mesoporosity, around 100 $m^2\ g^{-1}$, associated with a 40% increase of the mesopores effect (BJH values) when going from SiC-20 to SiC-60, as addressed above when considering the foam macroscopic skeleton densities.

Fig. 5a shows without ambiguity that these foams bear some vermicular mesoporosity induced only by the Si(HIPE) vermicular mesoporosity used as the hard template. Also, small angle X-ray scattering (SAXS) experiments have been performed on these samples. The spectra display a broad single peak, without

Table 1 Mercury intrusion porosimetry data

Materials	Intrusion volume/$cm^3\ g^{-1}$	Porosity (%)	Bulk density/g cm^{-3}	Skeletal density/g cm^{-3}
Si(HIPE)	10.90	92	0.08	0.98
SiC-20	1.40	78	0.56	2.53
SiC-30	1.90	73	0.47	2.37
SiC-40	0.93	68	0.7	2.2
SiC-60	0.35	42	1.2	2.0

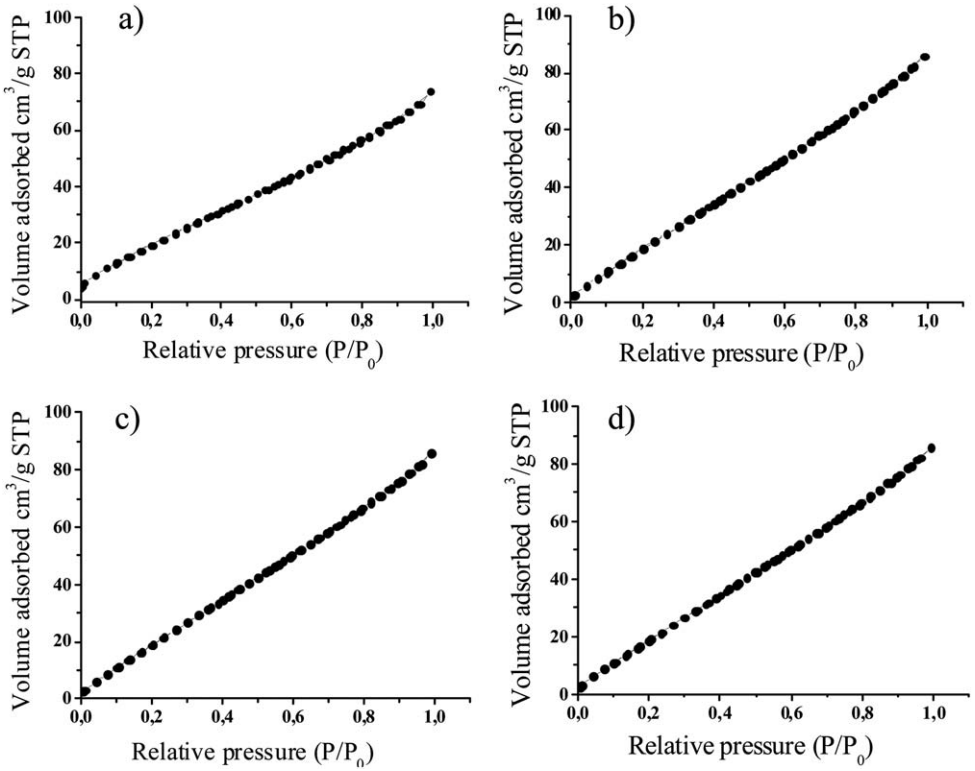

Fig. 3 Nitrogen sorption measurements of the SiC(HIPE): (a) SiC-20, (b) SiC-30, (c) SiC-40, (d) SiC-60.

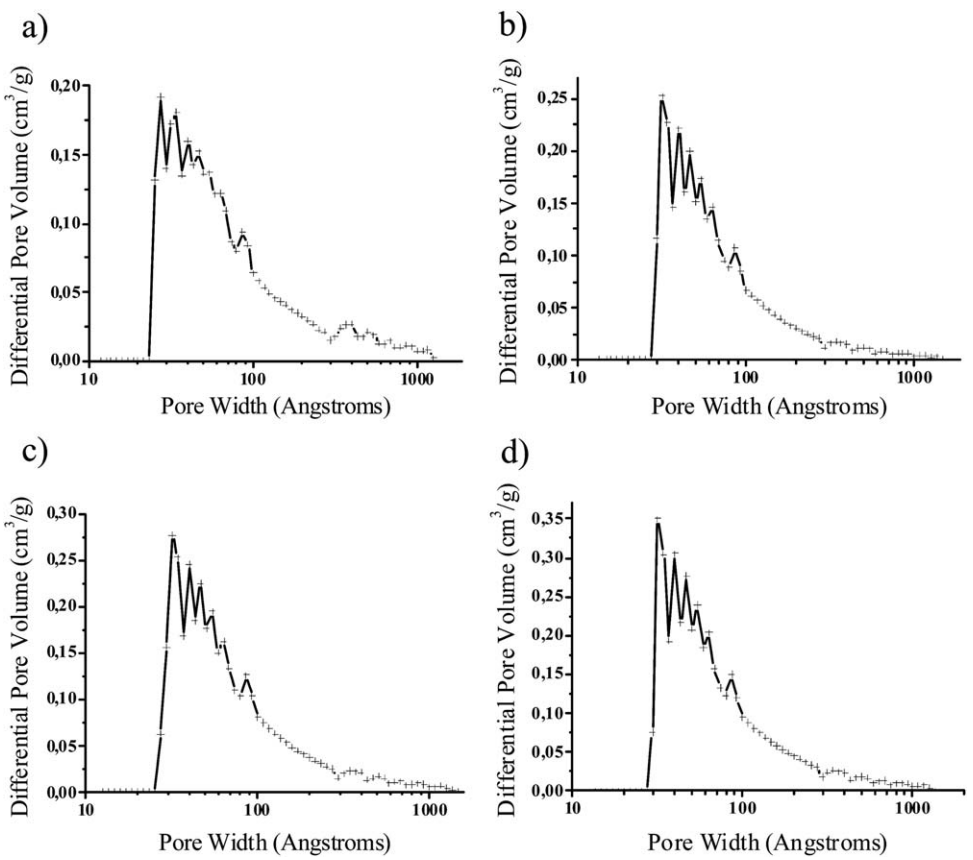

Fig. 4 Pore size distribution of the SiC(HIPE): (a) SiC-20, (b) SiC-30, (c) SiC-40, (d) SiC-60.

Table 2 β-SiC(HIPE) surface area calculated from nitrogen sorption measurements

Materials	BET/m^2 g^{-1}	BJH/m^2 g^{-1}	Total pore volume/cm^3 g^{-1}
Si(HIPE)	740	70.0	0.4
SiC-20	94	73	0.12
SiC-30	118	99	0.13
SiC-40	106	82	0.11
SiC-60	150	114	0.15

harmonics, centered at a wave vector of 0.19 $Å^{-1}$ corresponding to a wall-to-wall average distance of 4 nm (not shown here). This feature is characteristic of poorly organized nano-scopic void spaces, as can be observed on the TEM Fig. 5.

We have to note that the PCS impregnation route used here is lyotropic mesophase-free; this is to say without surfactant. In Fig. 5b we can see the β-SiC nanocrystals bearing a size between 2 and 4 nm. These nanocrystal sizes are the same when considering the Debye–Scherrer equation addressed for the XRD main peaks (Fig. 6). The X-ray diffraction (XRD) patterns of the resulting materials are shown in Fig. 6. Broad diffraction peaks around $2\theta = 35.6$, 42.1, 60.2, and 71.7° are ascribed to the (111), (200), (220) and (311) planes of cubic form silicon carbide (β-SiC).[24]

Also, all the IR spectra of the SiC(HIPE) foams exhibit a strong band at 830 cm^{-1} that is associated with the Si–C bond stretching mode, which further confirms the formation of silicon carbide (Fig. 7). Also, we can notice that the Si–O symmetric and asymmetric stretching modes present respectively at 1211 cm^{-1} and 1077 cm^{-1} (Fig. 7a) are mostly lost through the HF etching process, associated with the starting Si(HIPE) hard template dissolution. Despite HF washing, we can observe some weak remaining Si–O bands in the region 1200–1100 cm^{-1} (Fig. 7b–e), implying that residual oxygen is still present after the thermal and HF treatments. This point is discussed later using dispersive XPS.

The chemical composition was evaluated by elemental analysis and reveals that SiC(HIPE) foams contain silicon, carbon and oxygen (Table 3). The Si/C molar ratio varies between 0.61 and 0.72. Indeed, SiC ceramics obtained by the pyrolysis of PCS always contain carbon in excess and have a low Si/C molar ratio.[18] Typically, TG analysis of the representative as-synthesized SiC samples shows three steps of weight changes (Fig. 1, supplemental†). The first step, a gradual weight loss from 25 to 200 °C, corresponds to the loss of water adsorbed. The following weight loss from 300 to 600 °C is ascribed to the combustion of residual carbon. Then the third step, a gradual weight increase from 600 °C above, is due to the oxidation of SiC.

As discussed within the FTIR characterization section (Fig. 7) and shown through elemental analysis (Table 3), the SiC(HIPE) materials contain residual oxygen. We have thus performed surface characterization of these SiC(HIPE) foams using XPS analyses, bearing in mind that XPS is only a surface semi-quantitative method of investigation (Fig. 8). As observed in Fig. 8a, the Si_{2p} dominating signal centered at 100.8 eV confirms the predominance of SiC, in association with residual SiC_3O and SiC_2O_2 oxycarbides.[25] Also, when focusing on the C_{1s} signal (Fig. 8b), the presence of diverse carbon heteroatoms at the surface of these SiC(HIPE) monolithic foams is evidenced. As said before, ceramics obtained by the pyrolysis of PCS always contain excess carbon,[18] the excess carbon position also being present at the SiC external surface. As XPS is intrinsically a surface characterization technique, the Csp_2 signal will dominate, as is the case here.

Generating monolithic SiC(HIPE) foams is an important task to reach, but on the other hand if the as-synthesized foams' mechanical properties are poor, the added value of such

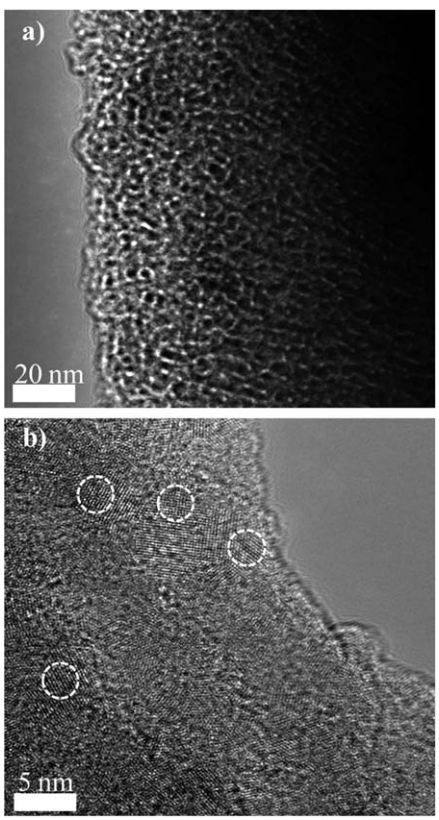

Fig. 5 SiC-40 example of vermicular mesoporosity: (a) using transmission electron microscopy (TEM) and β-SiC crystallites, and (b) using high resolution TEM where β-SiC crystallites can be observed within dashed circles.

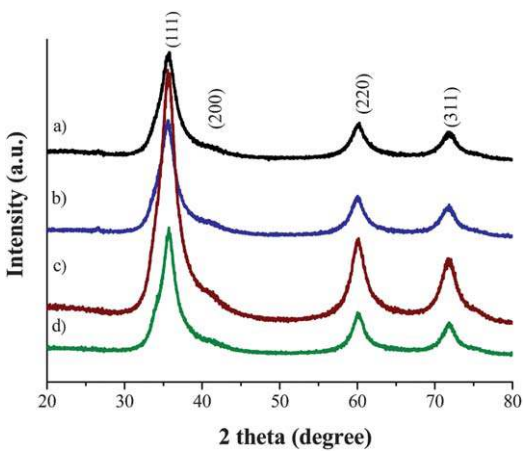

Fig. 6 XRD patterns of SiC(HIPE) treated at 1300 °C under argon after the removal of the silica framework: (a) SiC-60, (b) SiC-40, (c) SiC-30, (d) SiC-20.

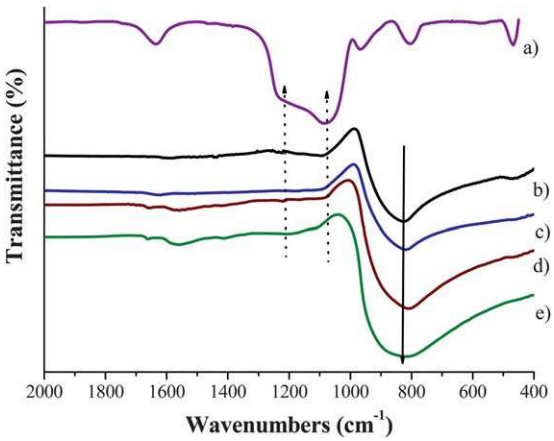

Fig. 7 IR spectra: (a) SiO_2, (b) SiC-60, (c) SiC-40, (d) SiC-30, (e) SiC-20.

Table 3 SiC(HIPE) composition addressed through elemental analysis

Materials	Si wt%	C wt%	O wt%	Si/C molar ratio
SiC-20	59.49	37.92	2.59	0.67
SiC-30	62.46	33.81	3.73	0.78
SiC-40	58.82	39.33	1.85	0.64
SiC-60	57.65	40.78	1.57	0.61

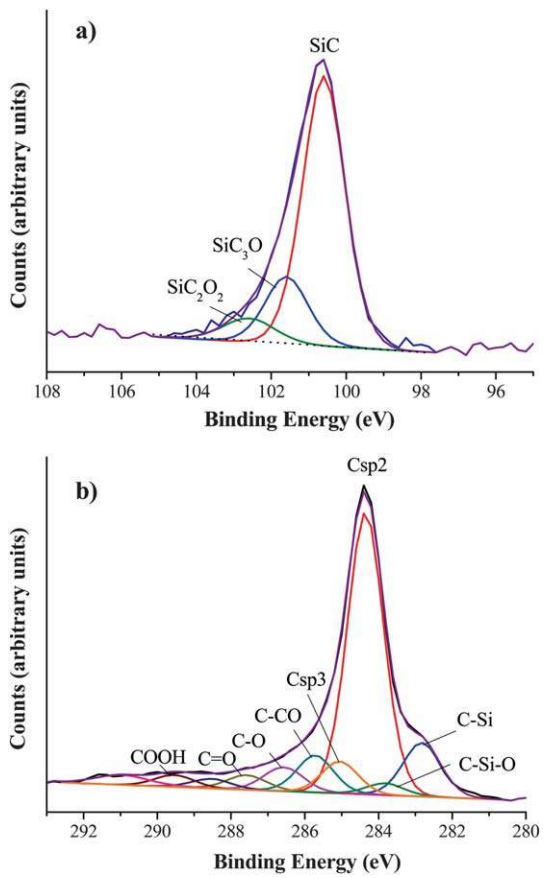

Fig. 8 Representative XPS surface analysis for the SiC-40 foam: (a) focus over the Si_{2p} region, (b) focus over the C_{1s} region.

materials will be reduced. We first notice that cutting the as-synthesized SiC(HIPE) monoliths by hand was impossible, particularly for the compounds obtained with the highest amounts of PCS precursor, where a diamond hand saw was needed to cut these monoliths precisely. This is the reason why we checked the mechanical properties of these compounds (Fig. 9).

As observed in Fig. 9, the curve of stress *vs.* strain for the SiC-30 material bears crenels. These crenels, where the stress decreases abruptly, are due to the macroporous texture and indicate that, statistically, under pressure, some macroporous walls collapse locally. This behavior is the same as the one observed recently for Carbon(HIPE) macroporous foams bearing the same hollow sphere aggregated morphology.[11] When the cellular foam walls become more continuous, *i.e.* when the PCS precursor concentration is increased (Fig. 2c and 2d), these crenel characteristics are lost for the SiC-40 and SiC-60 foams. As a direct consequence, the strain at rupture is decreasing from the SiC-30 to the SiC-60 foams. The average Young modulus values extracted from these compressions mechanical test are 50, 54 and 58 MPa respectively for the SiC-30, SiC-40 and SiC-60 foams respectively. If these Young modulus are 10 times lower than the one reached previously for Carbon(HIPE) partially graphitized,[11] they are 10–100 times higher than the best mechanical Young modulus obtained up to now for SiC monolithic porous materials.[26]

In order to extend the study of these foam physical properties as a function of their porosity we have also addressed thermal behaviors. We first have conducted some static DSC thermal analyses in order to obtain the foams heat capacity c_p *versus* macroporosity. These experiments which consist of submitting the sample to a temperature sine wave of a given amplitude and

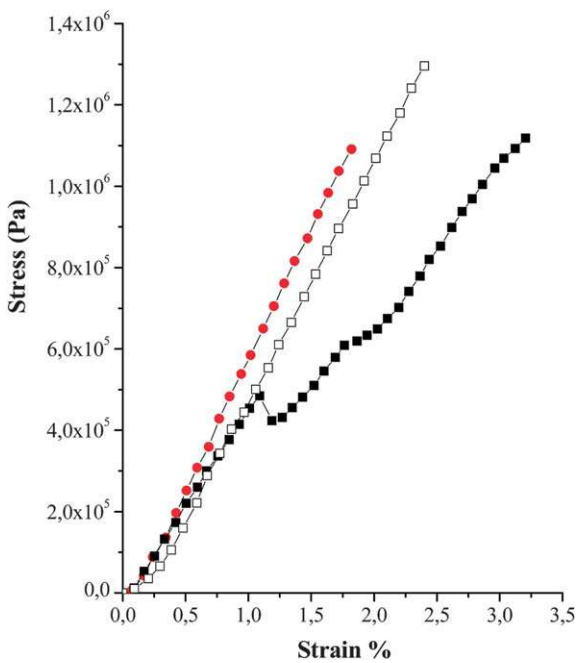

Fig. 9 Typical stress *versus* strain compression mechanical properties of the as-synthesized SiC(HIPE) monoliths: (■) SiC-30, (□) SiC-40, (●) SiC-60. The mechanical strength of the SiC-20 foams was not high enough to afford mechanical compression tests.

period intend to give a quasi-isothermal measure of the specific heat capacity (an example of the measurement is proposed within the supplemental section, Fig. S2†). The samples were prepared by cutting a single piece from the bulk material trying to match the masses of the three samples as much as possible. On the other hand we had no control over the surface area in contact with the aluminium calorimeter. Also, since we are dealing with heterogeneous samples with various morphologies, the purpose of this work is not to provide an accurate measure of the absolute heat capacity. Nevertheless applying a systematic protocol the results sound reasonably reliable in view of comparison of what we name the "bulk heat capacity" of the various materials.[27] As observed within Table 4, the foam bulk calorific capacities decrease when the foams porosity is increased.

In a second set of experiments each piece was crushed and the powder rerun under the same conditions. In such conditions we aimed to reach the SiC(HIPE) skeleton calorific capacities, bearing in mind that even in a powdered state there are still random interparticle void spaces. Anyway, in a such configuration the SiC(HIPE) pseudo-skeleton calorific capacities are converging to the value of 0.6 J g^{-1} K^{-1}, this value being close to the one provided in the literature, 0.67 J g^{-1} K^{-1}.

In addition to heat capacities, thermal diffusivities are quantities of interest. Neglecting convective heat losses from the surface, the temperature field at the surface evolves with time according to the following formula,[29]

$$\theta(r,t) = \frac{q}{4\pi\lambda r} erfc\left(\frac{r}{\sqrt{4at}}\right), \quad (1)$$

where $\theta(r,t) = T(r,t) - T_0$ is the temperature in excess above the ambient (K), q is the heat power (W m^{-3}), λ is the heat diffusivity (W m^{-1} K^{-1}), and $a = \lambda/(\rho c_p)$ is the heat diffusivity (m^2 s^{-1}) and *erfc* is the complementary error function. In the limit of r^2/t tending to large values, the *erfc* term tends to 1, allowing identification of the thermal conductivity by fitting $q/4\pi\theta$ *versus* r. However, in addition to this method, identification of the thermal *diffusivity*, a, is also possible by correlating the time derivative of the temperature to its apparent 2D Laplacian, without knowledge of the laser power or calibration of the IR camera signal.[28] Indeed, eqn (1) is a solution of the heat equation:

$$\frac{\partial\theta}{\partial t} = a\Delta\theta = a\left(\frac{\partial^2\theta}{\partial x^2} + \frac{\partial^2\theta}{\partial y^2} + \frac{\partial^2\theta}{\partial z^2}\right), \quad (2)$$

subject to the appropriate boundary and initial conditions, *i.e.* $\theta(r,0) = \delta(r)$and $\theta(\infty,t) = 0$. Here Δ symbolizes the Laplacian operator and δ the Dirac distribution. During the test, there exist time and position values for which, at the surface ($z = 0$), the z-directional term of the Laplacian $\frac{\partial^2\theta}{\partial z^2}$ is negligible with respect to the 2D Laplacian $\frac{\partial^2\theta}{\partial x^2} + \frac{\partial^2\theta}{\partial y^2}$, that can be measured from image processing at the surface. When this occurs, the heat diffusivity is retrieved by plotting the time derivative with respect to the 2D Laplacian. To implement this method, image processing operations have been performed. First, the image is corrected for projections, so that the spot image becomes circular. Then, the 2D Laplacian operator has been obtained at every point for each frame by convolution with a 5 × 5 standard mask; the time difference is obtained by direct frame subtraction. All quantities have been smoothed with respect to time, and averaged along a radial profile taken across the spot, excluding the region of the spot itself. The 2D Laplacian is plotted as a function of the time derivative; when a linear relation is obtained, the proportionality constant (*i.e.* the curve slope) is taken as the thermal diffusivity. Tracking the correlation between the time evolution and the Laplacian, we find curves with two neatly distinct slopes (see Fig. 10).

For low values of the 2D Laplacian, a 2D heat equation approximates the material behavior well, and we can capture the diffusivity, which is between 31 and 7 mm^2 s^{-1}. Using the bulk density and heat capacity values as given, one has tentative values of the heat conductivity $\lambda = a \cdot \rho \cdot c_p$ as low as 2.6 W m^{-1} K^{-1}, increasing with density (Table 4). We have also identified the conductivities directly by using eqn (1). Values are within 30% error with respect to the previous method. Our measured

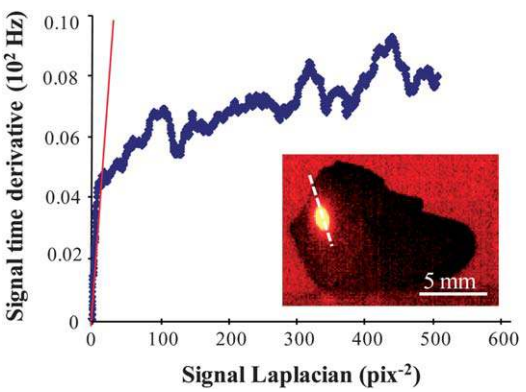

Fig. 10 Example of heat diffusivity measurement for the foam SiC-20. Averaged over a profile selected across the spot, values of the computed time derivative and of the Laplacian are plotted against each other: the initial slope (straight line) gives the heat diffusivity. The inset image gives an example of the IR image before correction and analysis where the white dashed line represents the whole radial heat path.

Table 4 Evolution of the SiC(HIPE) thermal properties with the percentage of porosity

Materials	% of porosity[a]	Heat capacity, c_p/J g^{-1} K^{-1}	Thermal diffusivity/mm^2 s^{-1}	Heat conductivity/W m^{-1} K^{-1}
SiC-20	78	0.15	31	2.6
SiC-40	68	0.22	25	3.9
SiC-60	42	0.55	7	4.6

[a] Values extracted from Table 1.

conductivities are in the same range as previously communicated ones (Table 4).[30] It may be rather surprising at first sight that even though the heat conductivity increases with density the thermal diffusivity decreases strongly; actually, this could be the sign of a complex role played by the pores, which may favor radiative heat transfer in addition to phonon propagation in the solid phase.

4. Conclusion

Through a hard templating method that makes use of Si(HIPE) as a hard monolithic mold to shape macro-mesoporous foams by using polycarbosilane as a pre-ceramic precursor, β-SiC macro/mesocellular foams have been synthesized. Both macroscopic plateau border (foam wall) morphology and final mechanical properties can be tuned through varying the starting amount of polycarbosilane precursor. The resulting silicon carbide foams, labeled SiC(HIPE), are composed of β-SiC at the microscopic length scale, while bearing 110 $m^2\ g^{-1}$ as the specific area at the mesoscopic length scale, and up to 92% of macroporosity. Surface characterization, using XPS investigations, has evidenced residual carbon and SiC_3O/SiC_2O_2 oxycarbides at the external surface of the foams' walls. The as-synthesized crack-free SiC(HIPE) monolithic foams are associated with outstanding mechanical properties as, for instance, 50–58 MPa of compression Young modulus. Considering these SiC foams' thermal behavior their bulk heat capacities (c_p) are increasing when the foams' porosity are decreasing, going from 0.15 J g^{-1} K^{-1} to 0.55 J g^{-1} K^{-1} respectively for the foams SiC-20 (78% of porosity) and the SiC-60 (48% of porosity). These foams' heat conductivities follow the same rules and increase when the foams' porosity decreases, going from 2.6 W m^{-1} K^{-1} to 4.6 W m^{-1} K^{-1} respectively for the foams SiC-20 (78% of porosity) and the SiC-60 (48% of porosity). These SiC macrocellular foams are associated with several applications ranging from catalyst supports to thermal and high frequency acoustic insulators.

Acknowledgements

We wish to thank Christine Labrugère and Eric Lebraud from ICMCB-CNRS for the XPS acquisitions and XRD measurements respectively, and Elisabeth Sellier (CREMEM) for TEM investigations. We also acknowledge the French ANR for financial support.

References

1 G. M. Whitesides and R. F. Ismagilov, *Science*, 1999, **284**, 89.
2 (*a*) R. Backov, *Soft Matter*, 2006, **2**, 452; (*b*) E. Prouzet, S. Ravaine, C. Sanchez and R. Backov, *New J. Chem.*, 2008, **32**, 1284; (*c*) N. Brun, S. Ungureanu, H. Deleuze and R. Backov, *Chem. Soc. Rev.*, 2011, **40**, 771; (*d*) C. Sanchez, P. Belleville, M. Popall and L. Nicole, *Chem. Soc. Rev.*, 2011, **40**, 696.
3 (*a*) F. Carn, A. Colin, M. F. Achard, H. Deleuze, E. Sellier, M. Birot and R. Backov, *J. Mater. Chem.*, 2004, **14**, 1370; (*b*) F. Carn, M. F. Achard, O. Babot, H. Deleuze, S. Réculusa and R. Backov, *J. Mater. Chem.*, 2005, **15**, 3887.
4 S. Ungureanu, M. Birot, G. Laurent, H. Deleuze, O. Babot, B. Julián-López, M. F. Achard, M. I. Popa, C. Sanchez and R. Backov, *Chem. Mater.*, 2007, **19**, 5786.
5 M. Destribats, V. Schmitt and R. Backov, *Langmuir*, 2010, **26**, 1734.
6 F. Carn, P. Masse, H. Saadaoui, B. Julian, H. Deleuze, S. Ravaine, C. Sanchez, D. R. Talham and R. Backov, *Langmuir*, 2006, **22**, 5469.
7 (*a*) Y. S. Hu, P. Adelhelm, B. M. Smarsly, S. Hore, M. Antonietti and J. Maier, *Adv. Funct. Mater.*, 2007, **17**, 1873; (*b*) L.-Z. Fan, Y. S. Hu, J. Maier, P. Adelhelm, B. Smarsly and M. Antonietti, *Adv. Funct. Mater.*, 2007, **17**, 3083.
8 S. Ungureanu, H. Deleuze, O. Babot, M. F. Achard, C. Sanchez, M. I. Popa and R. Backov, *Appl. Catal., A*, 2010, **390**, 51.
9 N. Li and K. Sabakie, *J. Membr. Sci.*, 2008, **314**, 183.
10 N. Brun, S. Prabaharan, M. Morcrette, C. Sanchez, G. Pécastaing, A. Derré, A. Soum, H. Deleuze, M. Birot and R. Backov, *Adv. Funct. Mater.*, 2009, **19**, 3136.
11 N. Brun, A. Babeau Garcia, H. Deleuze, M. F. Achard, C. Sanchez, F. Durand, V. Oestreicher and R. Backov, *Chem. Mater.*, 2010, **22**, 4555.
12 O. Regev, R. Backov and C. Faure, *Chem. Mater.*, 2004, **16**, 5280.
13 C. Boissière, D. Grosso, H. Amenitsch, A. Gibaud, A. Coupe, N. Bacile and C. Sanchez, *Chem. Commun.*, 2003, 2798.
14 (*a*) H. Klemm, M. Herrmann and C. Schubert, *J. Eng. Gas Turbines Power*, 2000, **122**, 13; (*b*) K. Watari, *J. Ceram. Soc. Jpn.*, 2001, **109**, S7.
15 (*a*) G. Q. Jin and X. Y. Guo, *Microporous Mesoporous Mater.*, 2003, **60**, 207; (*b*) J. Parmentier, J. Patarin, J. Dentzer and C. Vix-Guterl, *Ceram. Int.*, 2002, **28**, 1.
16 P. T. B. Shaffer, *Acta Crystallogr., Sect. B: Struct. Crystallogr. Cryst. Chem.*, 1969, **25**, 477.
17 A. G. Acheson, *British Patent*, 1892, 17911.
18 (*a*) Y. F. Shi, Y. Meng, D. H. Chen, S. J. Cheng, P. Chen, H. F. Yang, Y. Wan and D. Y. Zhao, *Adv. Funct. Mater.*, 2006, **16**, 561; (*b*) M. Birot, J.-P. Pillot and J. Dunogues, *Chem. Soc. Rev.*, 1995, **95**, 1443.
19 N. Leventis, A. Sadekar, N. Chandrasekaran and C. Sotiriou-Leventis, *Chem. Mater.*, 2010, **22**, 2790.
20 I. K. Sung, C. M. Mitchell, D. P. Kim and P. J. A. Kenis, *Adv. Funct. Mater.*, 2005, **15**, 1336.
21 K. Sonnenburg, Ph. Adelhelm, M. Antonietti, B. Smarsly, R. Nöske and P. Strauch, *Phys. Chem. Chem. Phys.*, 2006, **8**, 3561.
22 J. H. Eom and Y. W. Kim, *Met. Mater. Int.*, 2010, **16**, 399.
23 P. Colombo, *J. Eur. Ceram. Soc.*, 2008, **28**, 1389.
24 H. Jagodzinski, *Acta Crystallogr.*, 1949, **2**, 201.
25 Z. Liu, W. Shen, W. Bu, H. Chen, Z. Hua, L. Zhang, L. Li, J. Shi and S. Tan, *Microporous Mesoporous Mater.*, 2005, **82**, 137.
26 Y. W. Kim, Y. J. Jin, J. H. Eom, I. H. Song and H. D. Kim, *J. Mater. Sci.*, 2010, **45**, 2808.
27 *CRC Handbook of Chemistry and Physics*, 91st Edition, 2010–2011.
28 V. Ayvazyan, J.-C. Batsale and C. Pradere, in *QIRT 2010 Procs*, Maldague, X. P. V. ed., Editions du CAO, Les Eboulements, QC, Canada 2010, ref. 009.
29 H. S. Carslaw and J. C. Jaeger, *Conduction of Heat in Solids*, 2nd edn, Oxford University Press, 1959, p. 261.
30 N. B. Morley, Y. Katoh, S. Malang, B. A. Pint, A. R. Raffray, S. Sharafat, S. Smolentsev and G. E. Youngblood, *Fusion Eng. Des.*, 2008, **83**, 920.

Supplemental information

Tough Silicon Carbide Macro/Mesocellular Crack-Free Monolithic Foams

Simona Ungureanu,[1,2] Gilles Sigaud,[1] Gérard L. Vignoles,[3], C. Lorrette,[4,] Marc Birot,[2,*] Alain Derré,[1] Odile Babot,[2] Hervé Deleuze,[2]Alain Soum, [5] Gilles Pécastaings[5] and Rénal Backov[1,*]

[1] Université de Bordeaux, Centre de Recherche Paul Pascal, UPR 8641 CNRS, 115 avenue Albert Schweitzer, 33600 Pessac, France. E-mail: backov@crpp-bordeaux.cnrs.fr

[2] Université de Bordeaux, Institut des Sciences Moléculaires (ISM) UMR 5255 CNRS, 351 Cours de la Libération, 33405 Talence, France. E-mail: m.birot@ism.u-bordeaux1.fr

[3] Université de Bordeaux, Laboratoire des Composites Thermostructuraux, UMR 5801 CNRS-UB1-CEA-Snecma Propulsion Solide, 3 Allée de la Boétie, 33600 Pessac, France.

[4] CEA, Laboratoire des Composites Thermostructuraux, UMR 5801 CNRS-UB1-CEA-Snecma Propulsion Solide, 3 Allée de la Boétie, 33600 Pessac, France.

[5] Université de Bordeaux, Laboratoire de Chimie des Polymères Organiques UMR 5629 CNRS, ENSCBP 16 avenue Pey Berland, BP 108, 33607 Pessac, France.

1. TG Analyses

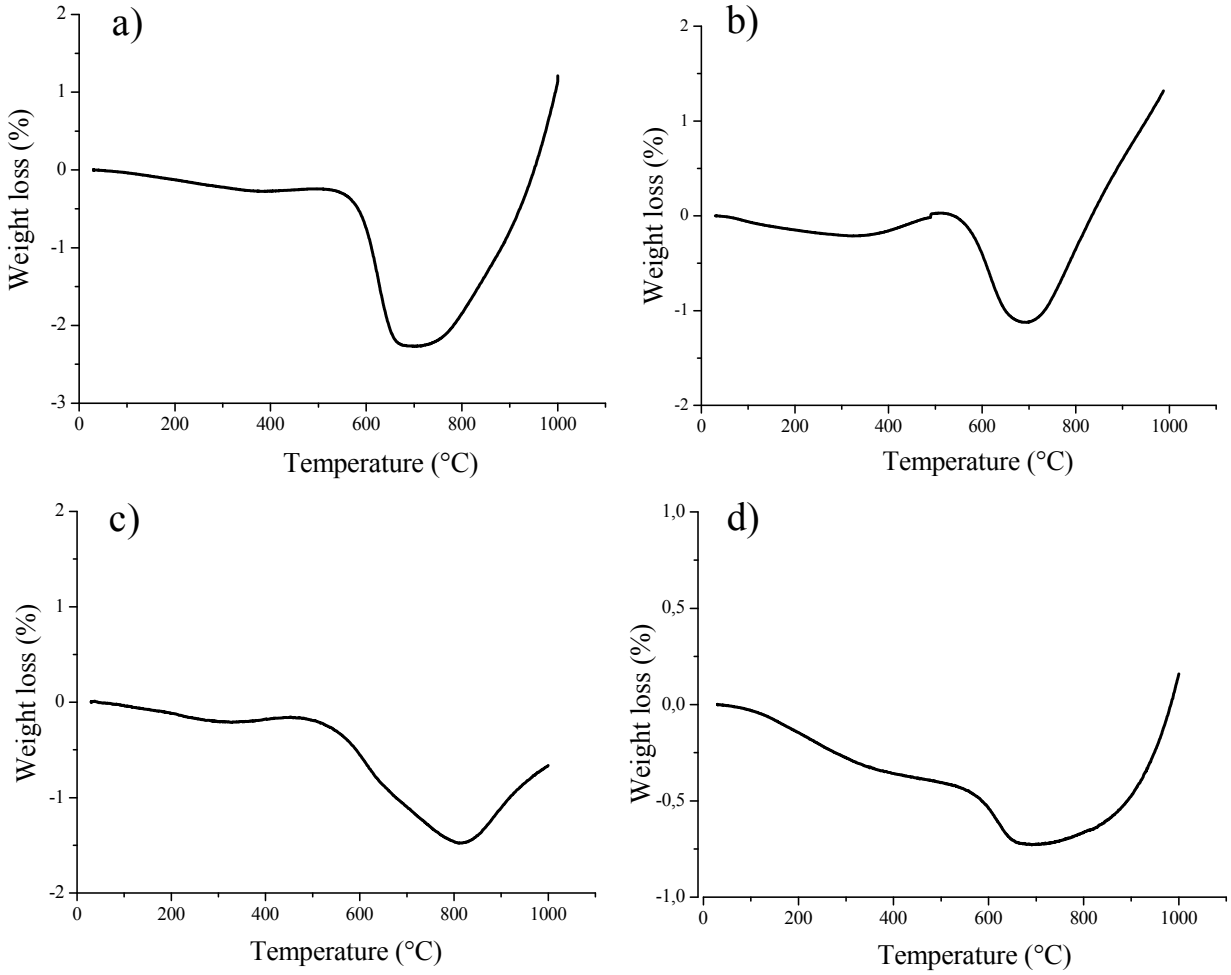

Figure S1. TG analysis under oxygen flow of the as-synthesized β-SiC(HIPE) samples: a) β-SiC-20, b) β-SiC-30, c) β-SiC-40, d) β-SiC-60.

2. DSC experiments

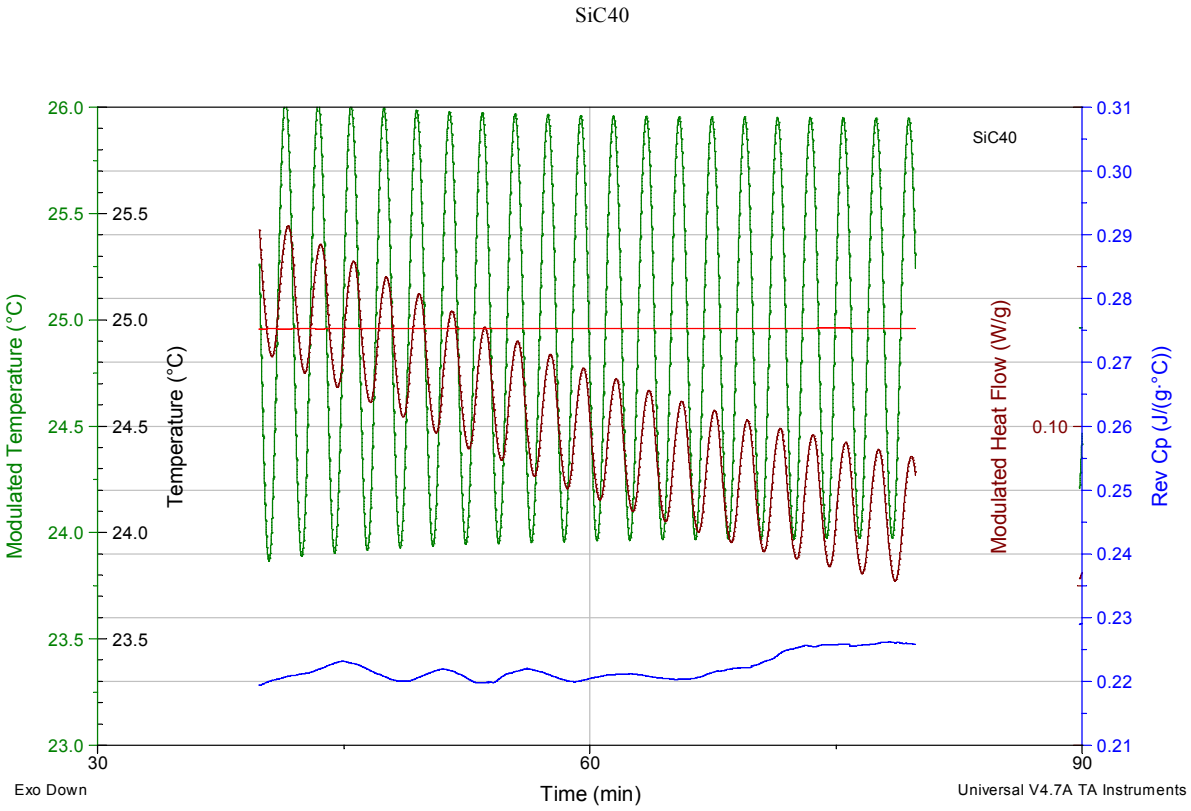

Figure S2. Example of a quasi isothermal heat capacity measurement in modulated temperature mode (β-SiC-40): the *bulk* C_P (bottom curve) is calculated from the temperature modulation ((25±1)°C, larger amplitude periodic curve) and the measured heat flux (smaller amplitude periodic curve).